TU Delft

Delft University of Technology

Parametric exploration of zero-energy modes in three-terminal InSb-Al nanowire devices

Wang, Ji Yin; Van Loo, Nick; Mazur, Grzegorz P.; Levajac, Vukan; Malinowski, Filip K.; Lemang, Mathilde; Borsoi, Francesco; Badawy, Ghada; Quintero-Pérez, Marina; Heedt, Sebastian

DOI
10.1103/PhysRevB.106.075306

Publication date
2022

Document Version
Final published version

Published in
Physical Review B

Citation (APA)
Wang, J. Y., Van Loo, N., Mazur, G. P., Levajac, V., Malinowski, F. K., Lemang, M., Borsoi, F., Badawy, G., Quintero-Pérez, M., Heedt, S., & Kouwenhoven, L. P. (2022). Parametric exploration of zero-energy modes in three-terminal InSb-Al nanowire devices. *Physical Review B*, *106*(7), Article 075306. https://doi.org/10.1103/PhysRevB.106.075306

Important note
To cite this publication, please use the final published version (if applicable).
Please check the document version above.

Copyright
Other than for strictly personal use, it is not permitted to download, forward or distribute the text or part of it, without the consent of the author(s) and/or copyright holder(s), unless the work is under an open content license such as Creative Commons.

Takedown policy
Please contact us and provide details if you believe this document breaches copyrights.
We will remove access to the work immediately and investigate your claim.

This work is downloaded from Delft University of Technology.
For technical reasons the number of authors shown on this cover page is limited to a maximum of 10.

Parametric exploration of zero-energy modes in three-terminal InSb-Al nanowire devices

Ji-Yin Wang,[1,*] Nick van Loo,[1] Grzegorz P. Mazur,[1] Vukan Levajac,[1] Filip K. Malinowski,[1] Mathilde Lemang,[1] Francesco Borsoi,[1] Ghada Badawy,[2] Sasa Gazibegovic,[2] Erik P. A. M. Bakkers,[2] Marina Quintero-Pérez,[1,3] Sebastian Heedt,[1] and Leo P. Kouwenhoven[1]

[1]*QuTech and Kavli Institute of Nanoscience, Delft University of Technology, 2600 GA Delft, The Netherlands*
[2]*Department of Applied Physics, Eindhoven University of Technology, 5600 MB Eindhoven, The Netherlands*
[3]*Netherlands Organisation for Applied Scientific Research (TNO), Delft 2600 AD, Netherlands*

(Received 3 February 2022; accepted 5 August 2022; published 30 August 2022)

We systematically study three-terminal InSb-Al nanowire devices by using radio-frequency reflectometry. Tunneling spectroscopy measurements on both ends of the hybrid nanowires are performed while systematically varying the chemical potential, magnetic field, and junction transparencies. Identifying the lowest-energy state allows for the construction of the lowest- and zero-energy state diagrams, which show how the states evolve as a function of the aforementioned parameters. Importantly, comparing the diagrams taken for each end of the hybrids enables the identification of states which do not coexist simultaneously, ruling out a significant amount of the parameter space as candidates for a topological phase. Furthermore, altering junction transparencies filters out zero-energy states sensitive to a local gate potential. Such a measurement strategy significantly reduces the time necessary to identify a potential topological phase and minimizes the risk of falsely recognizing trivial bound states as Majorana zero modes.

DOI: 10.1103/PhysRevB.106.075306

I. INTRODUCTION

Superconductor-semiconductor hybrids have attracted great interest in recent years for their potential applications in creating Majorana zero modes (MZMs) [1–3]. Extensive experiments have been carried out on such hybrid nanowires [4–11] and hybrid two-dimensional electron gases (2DEGs) [12–14]. Zero-bias peaks (ZBPs), observed at the ends of such hybrids, were initially considered as evidence for the existence of MZMs. However, such ZBPs could also originate from alternative trivial mechanisms, such as quasi-Majoranas [15], disorder [16–20], or a combination of Zeeman and Little-Parks effects [21]. On the other hand, end-to-end correlations are a unique property of paired MZMs in a topological superconductor, and could be used to distinguish MZMs from trivial Andreev bound states in three-terminal architectures [22–25]. Simulations taking into account the physical details of experimental devices (i.e., superconductor-semiconductor coupling, band offset at the interface, multiple subbands, and disorder effects) predict a significantly reduced and complex topological phase space [26]. Therefore, finding such a phase in the large parameter space requires the development of a detection method capable of scanning the entire parameter space within a practical time [27]. Radio-frequency (rf) techniques have been succesfully implemented on superconducting qubits [28], spin qubits [29], and hybrid devices [30,31]. Compared to traditional dc conductance measurements, it enables a fast and high-resolution exploration of all essential parameters in hybrid devices.

Three-terminal InSb-Al nanowire devices are systematically investigated using rf reflectometry. Local tunneling spectroscopy is performed at two ends of the hybrid nanowires, while exploring the chemical potential (controlled by the so-called 'super gate') and external magnetic field. The lowest-energy states (LESs) and zero-energy states (ZESs) are extracted as a function of super gate voltage and magnetic field, forming LES or ZES diagrams. As MZMs in an idealized model feature end-to-end correlations, the extracted diagrams of the two sides are compared to filter out uncorrelated ZESs. Stability of ZESs to transparency variation is studied by altering barrier gate settings, and zero-energy Andreev states residing around junctions are successfully identified. In addition, induced superconductivity on two ends of the hybrid nanowires is extracted, helpful for quantifing superconductor-semiconductor coupling in the hybrid nanowires. By applying the aforementioned experimental procedure, typical patterns of ZBPs are identified in the studied devices, but after a closer inspection nontopological explanations are more likely. The approach is able to significantly accelerate the identification on a potential topological phase.

II. EXPERIMENTAL SETUP

Figure 1(a) shows a circuit diagram of the measurement setup together with a false-color scanning electron microscope (SEM) image of device 1. Three-terminal devices are fabricated from InSb nanowires [32] using the recently developed shadow-wall lithography technique, enabling high-quality semiconductor-superconductor quantum devices [33,34]. In the SEM image, an Al film (blue) is connected from the substrate to the nanowire to serve as a superconducting drain

*wangjiyinshu@gmail.com

 ©2022 American Physical Society

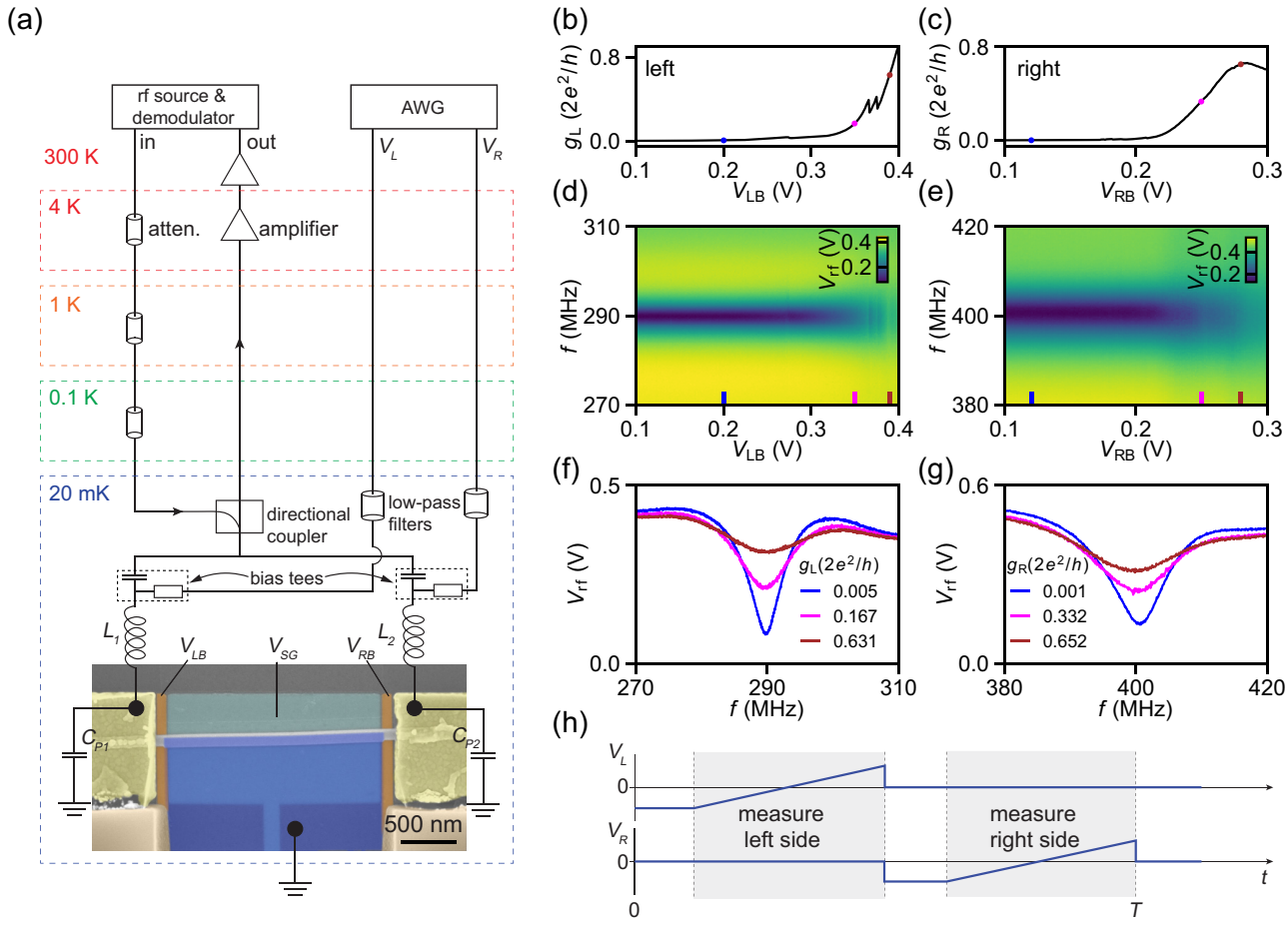

FIG. 1. Rf reflectometry measurement setup and its basic characteristics. (a) Measurement circuit together with a false-color SEM image of a three-terminal InSb-Al device. The superconducting lead (blue) is made from Al, connecting from the substrate to the nanowire. The superconductor-semiconductor hybrid is ∼2 μm long. Two probe leads (yellow), made from Ti/Au, are bonded to two superconducting inductors L_1, L_2. Voltages V_{LB} and V_{RB} are applied to bottom gates (orange) for tuning the left and right tunneling barriers, respectively. The chemical potential of the hybrid nanowire is tuned by the super gate (turquoise) with voltage V_{SG}. [(b) and (c)] Dc conductance of left and right junction (g_L, g_R) versus corresponding barrier gate voltage (V_{LB}, V_{RB}). [(d) and (e)] Corresponding rf response as a function of barrier gates in the same range as (b) and (c). [(f) and (g)] Line cuts at specific gate voltages from (d) and (e). In (d)–(g), V_{rf} is the amplitude of the reflected rf signal with ∼30 dB amplification at 4 K and ∼65 dB amplification at room temperature. (h) Bias-voltage waveforms applied at two probe leads as a function of time. In the shaded time period, voltage-bias spectroscopy of either side is performed. T is the time period for measuring bias-spectroscopy traces on both sides.

lead, while Ti/Au contacts (yellow) are fabricated on both ends of the hybrid nanowire to serve as probe leads. Voltages V_{LB} and V_{RB} are applied onto barrier gates (orange) to tune the transparency of the tunneling junctions. The voltage on the super gate (turquoise), V_{SG}, is changing the chemical potential of the hybrid nanowire. In Fig. S1 in Ref. [35], we show SEM pictures of two additional measured devices and a schematic of the cross-section of the device. The hybrids in all three devices are ∼2 μm long.

In order to accelerate tunneling spectroscopy at both junctions, an rf-conductance measurement scheme is employed [30,36,37]. The left and right probe lead of the device are connected to two superconducting spiral inductors (L_1, L_2) [29]. Together with parasitic capacitors (C_{P1}, C_{P2}) to ground, the inductors form two rf resonant circuits with typical resonance frequencies 250–450 MHz (see optical images of inductor chips with devices in Fig. S2 [35]). Each resonator acts as an impedance transformer for the corresponding tunneling junction. On resonance, the typical junction impedance (∼150 kΩ) is converted towards 50 Ω, which is the characteristic impedance of the transmission lines in the cryostat. Consequently, the reflection of the rf circuits at resonance displays a sensitive dependence on the differential conductance of the tunneling junctions. Figures 1(b) and 1(c) present the pinch-off curves of the junctions at the two ends of the hybrid nanowire, at 10 mV dc bias, while Figs. 1(d)–1(g) show corresponding response of the resonator circuits. The rf reflection has a sensitive response to conductance changing from 0.005 G_0 to 0.6 G_0 (G_0=$2e^2/h$). Such a broad conductance response allows sensitive rf detection at different tunneling transparencies.

The integration time per data point is about 1 ms, approximately two orders of magnitude less than the integration time of a conventional lock-in conductance measurement. To take advantage of the reduced integration time, we employ a rastering scheme [37,38] to rapidly sweep the dc voltage

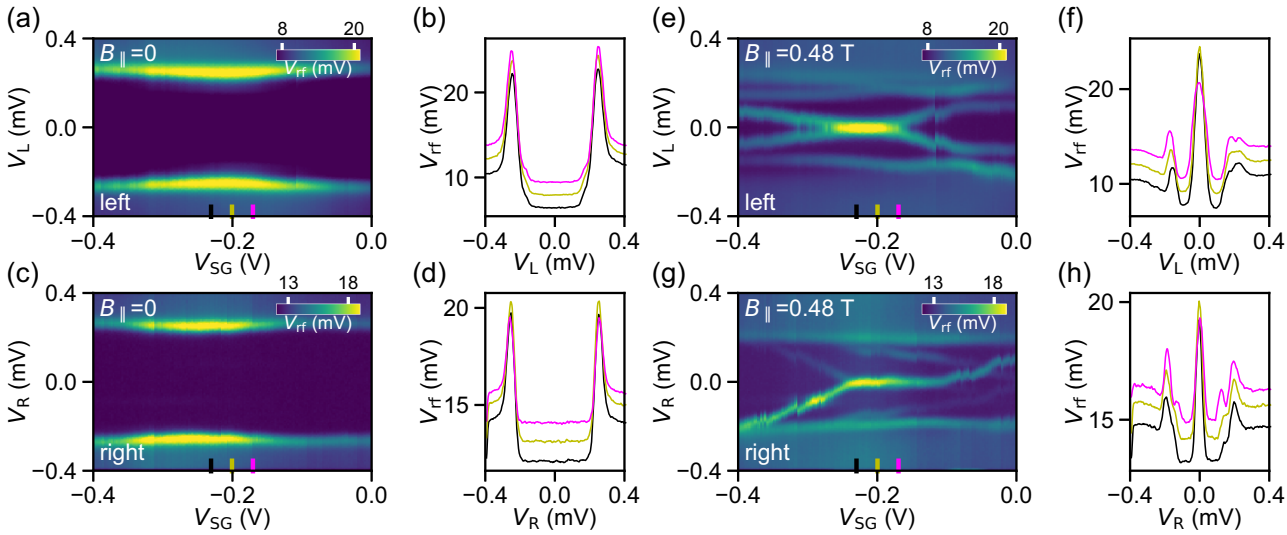

FIG. 2. [(a) and (e)] Selected segments of tunneling spectroscopy at the left junction at $B_{||} = 0$ T and $B_{||} = 0.48$ T, respectively. Line cuts are taken at colored bars and shown in (b) and (f). (c) and (g) are similar as (a) and (e), but for the right junction. (d) and (h) show line cuts from (c) and (g). Line cuts at zero magnetic field show a hard gap on both sides. Results at $B_{||} = 0.48$ T illustrate the coexistence of zero-bias peaks on two sides. Note that the curves shown in (b), (d), (f), and (h) are shifted vertically for better visibility.

bias applied at the tunneling junctions. Figure 1(h) shows the waveforms generated by an arbitrary waveform generator (AWG). To perform the tunneling spectroscopy measurements at the two ends of the nanowire, the AWG generates a pair of triangular pulses, each sweeping the dc voltage bias at one of the junctions. The waveforms are accompanied by triggers, synchronizing the data acquisition with the voltage sweeps. Throughout the experiment, we perform pairs of tunneling spectroscopy measurement (typically 200 data points for each side with a total duration of ∼0.4 s), which we repeat while varying gate voltages and the external magnetic field.

III. RESULTS

A. Tunneling spectroscopy

Initially, basic characterization of devices and resonators is performed before moving to tunneling spectroscopy with rf. First, cross-talk between the super gate and barrier gates is measured at a fixed dc voltage bias. While sweeping V_{SG}, barrier gate voltages are changed accordingly to maintain a constant junction conductance (see Figs. S3(a) and S3(b) in Ref. [35]). Next, the magnetic field is aligned along the nanowire axis. Furthermore, the resonator frequency shift in an external magnetic field is characterized (see Figs. S3(c) and S3(d) in Ref. [35]). As the external magnetic field is swept, the probing frequencies are adjusted to maintain a high sensitivity of the rf conductance measurement. Finally, tunneling spectroscopy is performed on both sides of the device by applying the dc bias waveform illustrated in Fig. 1(h), while stepping V_{SG} and the parallel magnetic field, $B_{||}$.

Figure 2 shows segments of tunneling spectroscopy measurements on two nanowire ends at different $B_{||}$. Figures 2(a) and 2(c) show the results as a function of V_{SG} at $B_{||} = 0$. Line cuts at different V_{SG} are presented in Figs. 2(b) and 2(d). Suppressed conductance in between two pronounced coherence peaks suggests a hard superconducting gap. The superconducting gap is ∼260 μeV, consistent with previous report based on the same fabrication platform [33,34]. Figures 2(e) and 2(g) present an example of subgap features

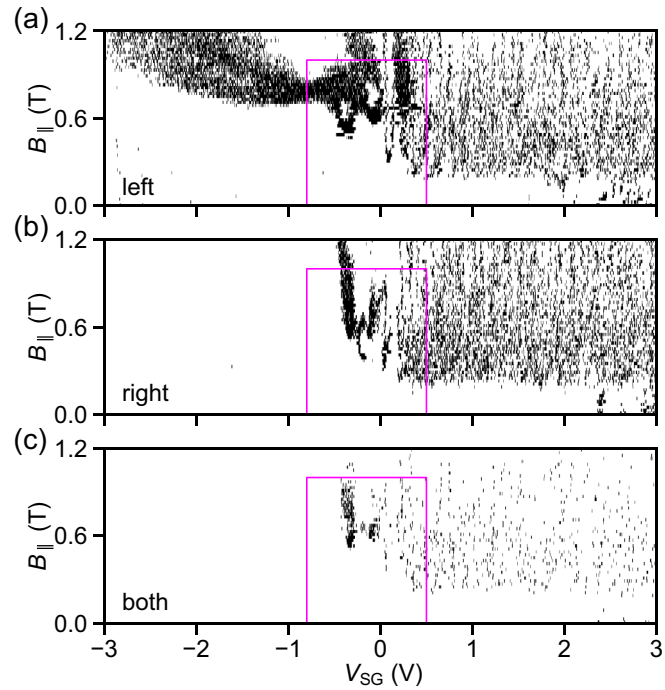

FIG. 3. ZES diagrams as a function of V_{SG} and $B_{||}$ for the left (a) and right (b) junctions. Black and white pixels indicate the presence and absence of ZESs, respectively. (c) Diagram with black pixels indicating the coexistence of ZESs on both ends. In each panel, there are 2523 data points along V_{SG} and 61 along $B_{||}$ (i.e., total number of pixels is 2523×61). The full data set is acquired in ∼142 hours. Magenta rectangles mark the region with a relatively large density of coexistent ZESs. Calibration measurements, including Figs. 1(d), 1(e) and Fig. S3 in Ref. [35], take ∼13.5 hours.

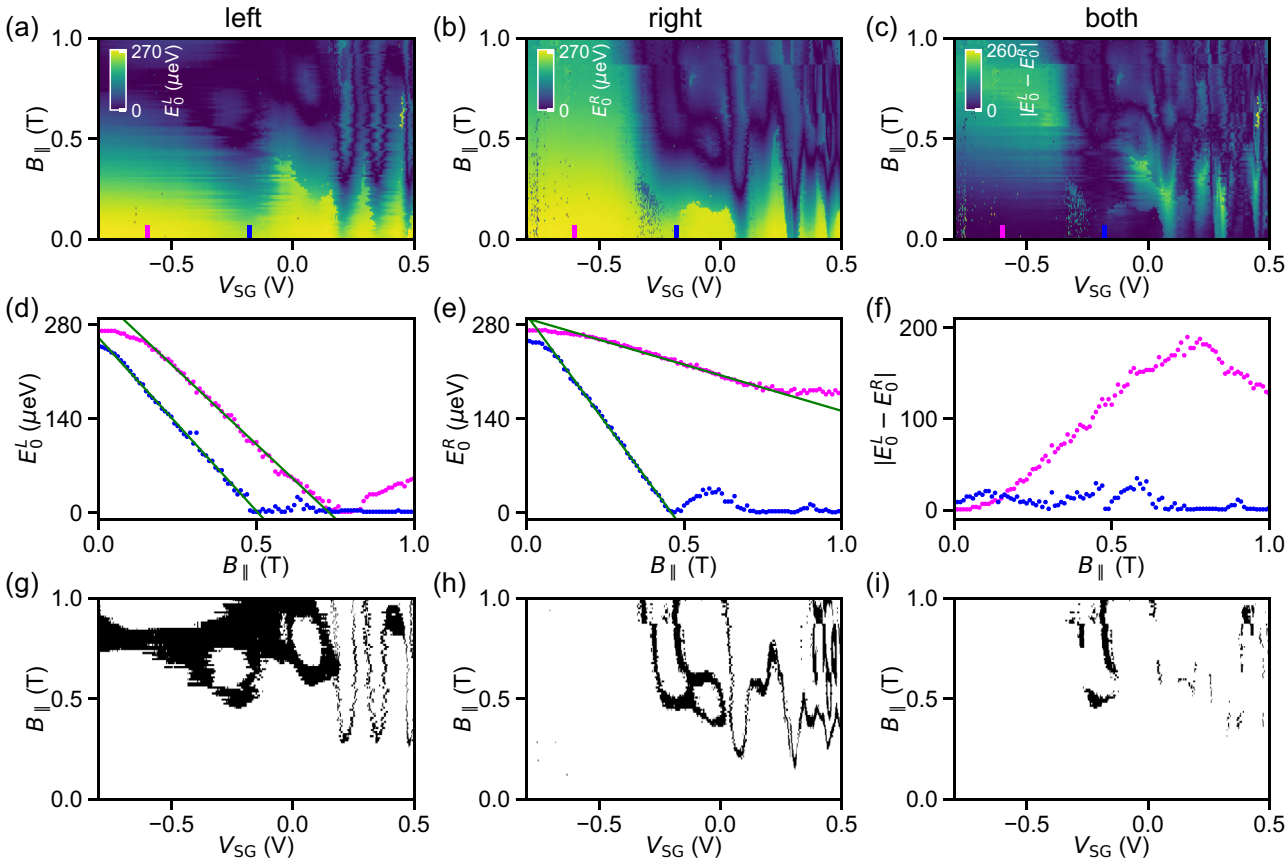

FIG. 4. High-resolution LES and ZES diagrams. (a) Energy of LESs, E_0^{L}, probed on the left junction as a function of V_{SG} and $B_{||}$. (b) Energy of LESs, E_0^{R}, probed on the right junction versus V_{SG} and $B_{||}$. (c) Energy difference between the LESs probed on the two ends. [(d)–(f)] Line cuts taken at different V_{SG} from (a)–(c). In (d) and (e), solid green lines are linear fits. (g) and (h) ZES diagrams for the left and right junction, respectively. (i) Diagram of coexisting ZESs on both ends. Gates are swept by following the cyan dashed lines ($g_{\mathrm{L}} \sim 0.035\ G_0$, $g_{\mathrm{R}} \sim 0.064\ G_0$) in Fig. S5 [35]. In (a)–(c) and (g)–(i), each panel includes 522 × 101 pixels. The dataset is acquired in ∼35 hours.

at $B_{||} = 0.48$ T for the same V_{SG} range as Figs. 2(a) and 2(c). ZBPs are formed at both ends between $V_{\mathrm{SG}} = -0.23$ V and $V_{\mathrm{SG}} = -0.15$ V [see Figs. 2(f) and 2(h) for line cuts]. ZBPs, peaks in differential conductance at zero energy, indicate the existence of ZESs, which are states with zero energy. Having established our setup for tunneling spectroscopy at both nanowire ends, we start mapping ZESs as a function of multiple parameters over a large range with high resolution.

B. Diagrams of lowest- and zero-energy states

For a given combination of $B_{||}$ and V_{SG}, the presence of ZBPs is validated by analyzing one V_{rf}-$V_{\mathrm{L/R}}$ trace (see Fig. S6 [35] for details). This is repeated for all measured parameter values and presented as ZES diagrams, as shown in Fig. 3. Figure 3(c) shows coexisting ZESs on both ends of the hybrid nanowire. In these diagrams, three distinct regimes can be observed. (1) For negative super gate voltages ($V_{\mathrm{SG}} < -0.8$ V), ZESs only appear at high magnetic field (on the order of $B_{||} = 0.8$ T) and there are no coexistent ZESs. (2) For positive super gate voltages ($V_{\mathrm{SG}} > 0.5$ V), ZESs are ubiquitous at fields as low as $B_{||} = 0.2$ T (An example of bias spectroscopy in this regime is shown in Fig. S4). Here, coexistent ZESs are sparsely distributed in parameter space. (3) In an intermediate regime (-0.8 V $< V_{\mathrm{SG}} < 0.5$ V), ZESs emerge at moderate magnetic fields compared to the other two regimes. Notably, ZESs form regular shapes in parameter space and there is a significant amount of coexisting ZESs. This behavior is reproduced for two other InSb-Al hybrid nanowires presented in this work (see Figs. S12 and S14 [35]). A recent work on InSb-Al hybrid islands reports three similar regimes in V_{SG} [39]. It is explained by a tunable superconductor-semiconductor coupling with V_{SG} [26,40,41]. The intermediate regime is identified to be the most promising region to search for a topological superconducting phase. We focus the subsequent measurements on this intermediate super gate regime (marked by magenta rectangles in Fig. 3).

Figure 4 presents high-resolution diagrams obtained in the intermediate super gate regime. Figures 4(a) and 4(b) show the energy of LESs probed at the two junctions, E_0^L and E_0^R, versus V_{SG} and $B_{||}$ (LES extraction method is shown in Fig. S6 [35]). At zero magnetic field, $E_0^{\mathrm{L/R}}$ is close to the superconducting gap (∼260 μeV). As $B_{||}$ increases, $E_0^{\mathrm{L/R}}$ starts to drop due to the emergence of subgap states. In order to illustrate the dependence of $E_0^{\mathrm{L/R}}$ on $B_{||}$, examples of two vertical line cuts are shown in Figs. 4(d) and 4(e). These are picked to illustrate two types of behavior: For the blue line cuts ($V_{\mathrm{SG}} = -0.18$ V), the behavior on both sides of the nanowire

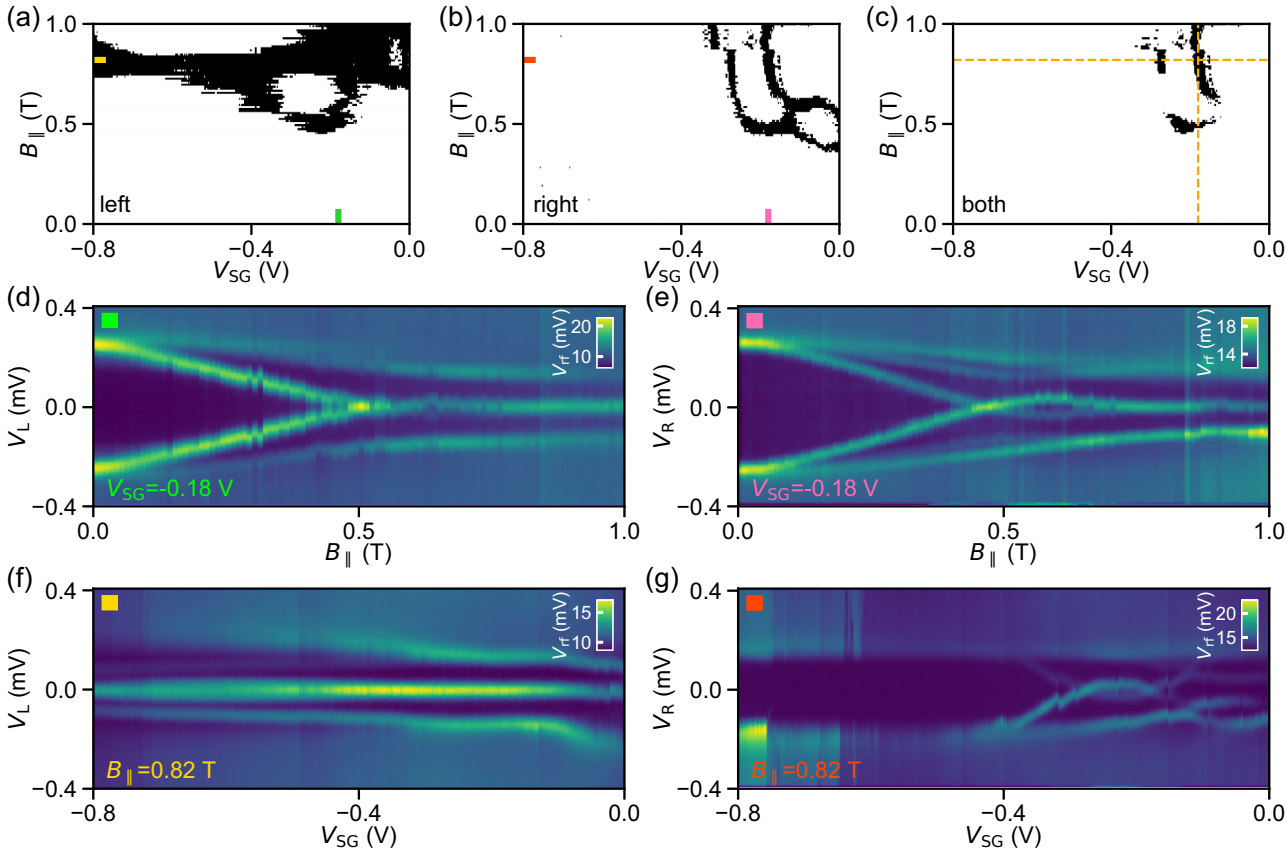

FIG. 5. Clusters of ZBPs with respect to super gate and magnetic field. [(a)–(c)] ZES diagrams for the left junction, the right junction, and coexistence in both junctions [same as Figs. 4(g)–4(i), but with reduced super gate range]. In (a), the green mark indicates the position of $V_{SG} = -0.18$ V and corresponding tunneling spectroscopy data is shown in (d). The results at $B_{||=0.82}$ T (yellow mark) is shown in (f). In (b), tunneling spectroscopy data of the vertical (pink mark) and horizontal (red mark) line cut is shown in (e) and (g), respectively. In (c), the horizontal and vertical dashed line indicates $B_{||} = 0.82$ T and $V_{SG} = -0.18$ V, respectively.

is similar. Subgap states emerge and drop to zero energy, with a comparable effective g factor (solid green lines are fitting traces to the linear part of the data). On the other hand, the magenta line cuts ($V_{SG} = -0.6$ V) show an example where on one junction, a subgap state drops to zero energy while on the other side no subgap states emerge. In order to identity LESs that may extend between the two ends of the hybrid nanowire, the energy difference between LESs, $|E_0^L - E_0^R|$, is calculated and shown in Fig. 4(c). Figure 4(f) shows the line cuts at the same V_{SG} as in Figs. 4(d) and 4(e). Notably, for the blue line cut, the energy difference of the LESs on both ends is close to zero within a large range of field, indicating a potential correlation. In contrast, the magenta line cut shows a large energy difference for almost all field values, which signifies uncorrelated behavior.

From the LES diagrams, states with zero energy are identified. These states are presented in ZES diagrams, shown in Figs. 4(g)–4(i) (see the example of the extraction process in Fig. S6 [35]). Similar to Fig. 3, black pixels in Figs. 4(g) and 4(h) represent the presence of ZESs, while white pixels indicate the absence of ZESs. Regular features are observed in these diagrams, including parabolic and oscillatory shapes, as well as clusters of black pixels. The intersection of the two diagrams yields a diagram [Fig. 4(i)] consisting of ZESs which coexist on both sides. Around $V_{SG} = -0.2$ V and $B_{||} > 0.5$ T, a high density of coexistent ZESs is observed which indicates a potential candidate region for a topological phase. In the following section, this region and several of the regular patterns will be further analyzed.

C. Detailed analysis of ZES and LES diagrams

1. Coexisting ZBP clusters

ZES diagrams constructed in the previous section identify a region with coexisting ZESs on both ends of the nanowire hybrid. Figures 5(a)–5(c) show a zoom-in of Figs. 4(g)–4(i). At fixed $V_{SG} = -0.18$ V, tunneling spectroscopy on both ends of the hybrid nanowire shows a subgap state reaching zero energy around 0.5 T [Figs. 5(d) and 5(e)]. After a single oscillation, it sticks to zero energy for ∼300 mT. On the other hand, when the magnetic field is fixed at 0.82 T, a stable ZES is observed only on the left side [Fig. 5(f)]. Remarkably, it persists for more than 800 mV in V_{SG}. Considering that the dielectric layer is made from 20 nm HfO_x, chemical potential is changed by a significant amount in this super gate range. Such stable ZBPs as a function of super gate voltage and magnetic field, together with similar behavior on both sides of the device as a function of magnetic field, have been previously

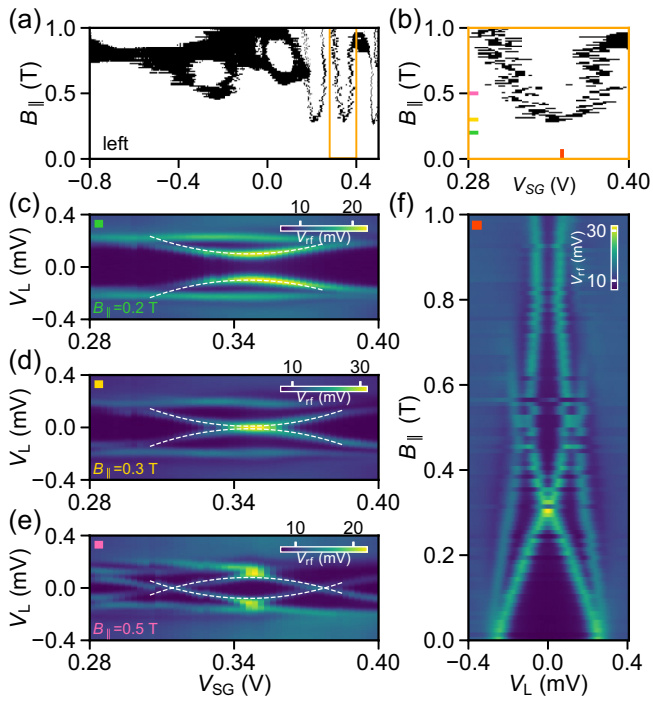

FIG. 6. Parabolic patterns in ZES diagrams. (a) ZES diagram for the left junction [same as Fig. 4(g)]. The region marked by the orange rectangle is replotted in (b). Three line cuts are made at different $B_{||}$ and corresponding tunneling spectroscopy data is displayed in [(c)–(e)]. White dashed lines serve as guide to the eye. (f) Evolution of subgap levels in magnetic field at $V_{SG} = 0.35$ V [red vertical line cut from (b)].

interpreted as evidence of MZMs. However, robust ZBPs can also originate from Andreev bound states formed in quantum dots near the junction [42], as well as due to disorder [20]. Indeed, tunneling spectroscopy along super gate on the right side of the device [Fig. 5(g)] reveals a strikingly different behavior, with only two crossings through zero energy. The different behaviors on the two sides of the device can be recognized as well from ZES diagrams in Figs. 5(a)–5(c). Such clearly distinct behavior with respect to changes in the chemical potential implies that the ZESs on the two sides of the device do not originate from an unbroken topological superconducting phase.

2. Parabolic patterns in ZES diagrams

In Fig. 4, ZESs form parabolic patterns in the V_{SG}-$B_{||}$ space. Such parabolic patterns can represent the onset of a topological phase when Majorana zero modes at two ends of a short hybrid nanowire strongly interact [9,43]. In Fig. 6, an example of such a parabola is shown and its tunneling spectroscopy data is presented. In Fig. 6(a), an orange rectangle marks the region with such a parabolic pattern. This region is replotted in Fig. 6(b). In order to understand the pattern, three line cuts are made at different magnetic fields and corresponding spectroscopic results are plotted in Figs. 6(c)–6(e). At $B_{||} = 0.2$ T [Fig. 6(c)], there is a pair of levels emerging below the superconducting gap, marked by white dashed lines. Once the magnetic field is increased to 0.3 T [Fig. 6(d)], the pair of subgap levels merges at zero energy, forming ZBPs. This field corresponds to the onset of ZESs in Fig. 6(b). At higher $B_{||}$, for example $B_{||} = 0.5$ T [Fig. 6(e)], the subgap levels form two crossings at zero energy. The evolution of these subgap levels in $B_{||}$ at $V_{SG} = 0.35$ V is shown in Fig. 6(f). In Fig. S7 [35], another parabolic pattern which has similar properties as Fig. 6 is presented. This behavior is fully explained by Zeeman-driven Andreev level splitting in a quantum dot proximitized by a superconducting lead [44].

3. Oscillatory patterns in LES diagrams

The oscillation of LESs in magnetic field with an increasing amplitude and period is consistent with the prediction of smoking gun evidence for MZMs [43]. This type of behavior would result in oscillatory patterns in LES and ZES diagrams. An example of such patterns is shown in Figs. 7(a) and 7(b). A line cut through such a circle, shown in Fig. 7(c) ($V_{SG} = -0.08$ V), shows the energy of a LES dropping to zero before oscillating with increasing amplitude and period, thus matching the smoking gun predictions. The tunneling spectroscopy data as a function of $B_{||}$ corresponding to this particular line cut is shown in Fig. 7(e). In this map, three discrete subgap states are observed and marked with an orange, white, and black lines. The LES (orange) first comes down in energy and crosses through zero energy, before interacting with another state (white). Interaction between these states results in an anti-crossing, which can be attributed to the mixing of different spin species of two states via spin-orbit interaction [45], and is represented by a gradient color. The LES crosses through zero once more, and subsequently interacts with another state (black). In addition, two spectroscopy results at a lower ($V_{SG} = -0.12$ V) and higher ($V_{SG} = -0.05$ V) super gate voltage are presented in Figs. 7(d) and 7(f), respectively. By changing the super gate voltage, the magnitude of the interaction between the states can be tuned. Consequently, the interactions can become negligible which results in states crossing rather than anticrossing. This indicates that the results in Fig. 7(e) or 7(c) arise from several subgap states interacting with each other. Thus, while the behavior of LESs in Figs. 7(e) and 7(c) is consistent with the predicted evidence of MZMs, such oscillations can originate from anti-crossings between the LES and other states. The analysis made above suggests that although oscillatory patterns in LES and ZES diagrams are expected for interacting MZMs, they may also originate from interactions between topologically trivial Andreev bound states.

4. Induced superconductivity

In addition to extracting the energy of various subgap states in the system, two other important parameters can be determined from the data: the superconducting gap size Δ and the effective g factor g^*. From the local tunneling spectroscopy measurements, the superconducting gap can be estimated by fitting zero-field $g_{L/R}$-$V_{L/R}$ traces with the BCS − Dynes formula [46], where $g_{L/R}$ is obtained from V_{rf}-$g_{L/R}$ correspondence in Fig. 1. On the other hand, the effective g factor is determined by making a linear fit to the energy dependence of the LES as a function of magnetic field [45,47]. In Fig. 8, the evolution of these two parameters is shown as a function of

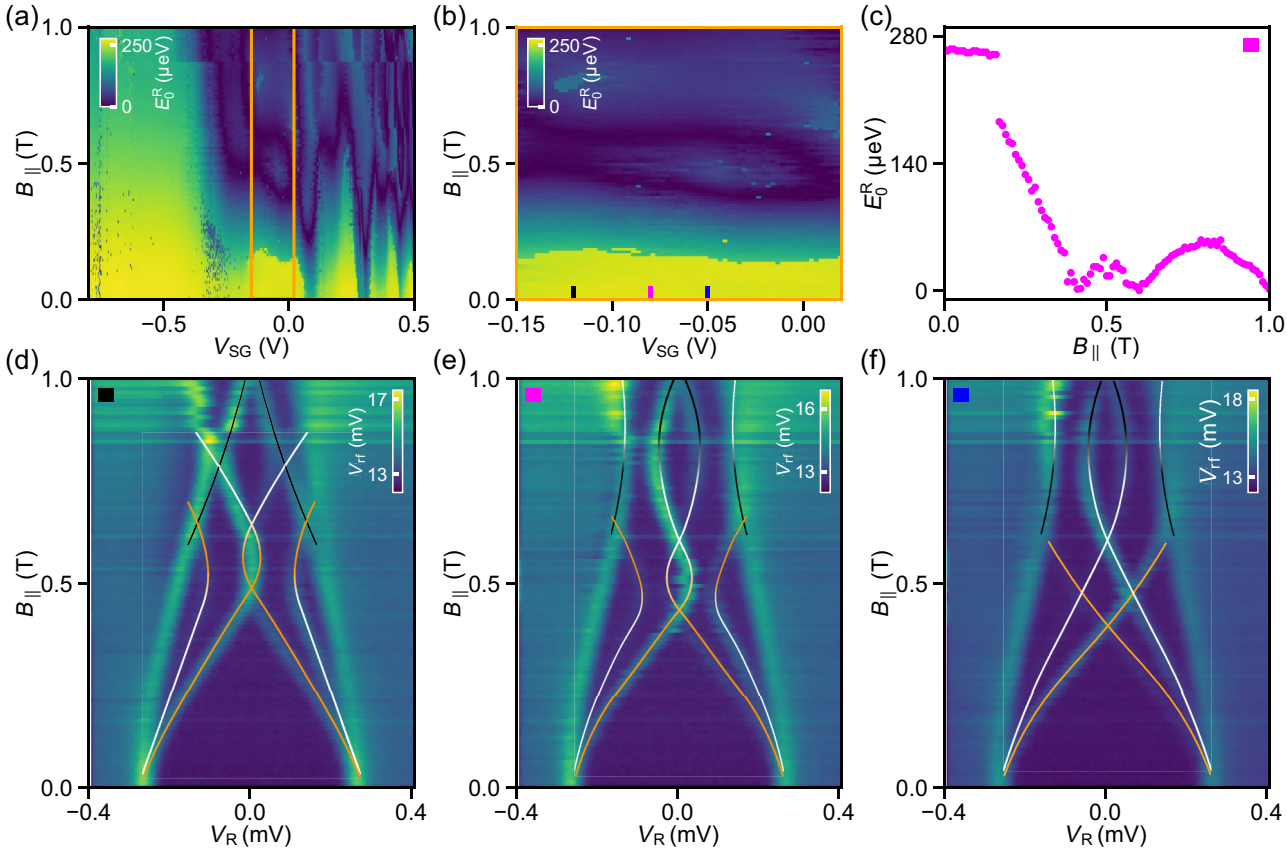

FIG. 7. Oscillatory patterns in LES diagrams. (a) LES diagram for the right junction (same as Fig. 4(b)). The region marked by the orange rectangle is plotted in (b). (c) Example of an oscillating LES, showing E_0^R vs $B_{||}$ for the line cut taken at $V_{SG} = -0.08$ V (marked by the magenta bar in (b)). Tunneling spectroscopy data taken at $V_{SG} = -0.12$ (black bar), -0.08 (magenta bar), and -0.05 V (blue bar) is shown in (d), (e), and (f), respectively. In (d)–(f), three subgap states are marked by orange, white, and black lines which serve as a guide to the eye. Gradient colors indicate interaction between states.

super gate voltage. At both ends of the nanowire, the estimated gap size behaves similarly and remains largely unaffected by the super gate. It only shows a small dip in the vicinity of $V_{SG} = -0.25$ V, and from the spectra shown in Fig. 2 it can be seen that these dips correspond to the energy minima of two LESs. However, if we instead look at the field evolution it becomes apparent that the extracted g factors do not behave in a similar way. This indicates that the LESs at two ends are uncorrelated. The right side of the device shows an absence of subgap states below $V_{SG} = -0.4$ V (see an example in Fig. S8 [35]). The corresponding g factor is estimated from the gap edge and remains close to 2, as the measured properties are dominated by the Al film. It is worth to note that with local tunneling spectroscopy, only the superconducting properties in the vicinity of the junctions are detected while leaving the bulk properties inaccessible. In contradiction to our observations, the induced gap size and effective g factor should behave similarly if they represent bulk properties [40]. Thus we conclude that the behaviors shown in Fig. 8 belong to Andreev bound states formed locally in the vicinity of the junctions [48]. Nonlocal measurements are required in order to investigate induced superconductivity, including gap closing, in the bulk of the hybrids [27].

D. Influence of barrier gates

ZESs formed in the vicinity of the junction can mimic MZM behavior with respect to magnetic field and chemical potential variations [49]. Tunnel transparency is an important experimental parameter which can be used for distinguishing MZMs from trivial Andreev bound states. To investigate the stability of ZESs shown in Fig. 4, similar measurements are performed with three different barrier gate settings. The corresponding processed diagrams are plotted in Figs. S9–S11 in Ref. [35]. ZES diagrams obtained for four different barrier gate settings are overlapped to form ZES histograms in Fig. 9. As shown in Fig. 9(a), the left end of the hybrid exhibits clusters of ZESs in the space of chemical potential and magnetic field. As those ZESs are stable against variation of all experimentally accessible parameters, they are compatible with MZMs. However, as shown in Fig. 9(b), the right side of the studied hybrid does not show similar stability and thus indicates that the device does not exhibit an unbroken topological superconducting phase. As expected, the uncorrelated behavior between left and right end of the hybrid is recognized as well in the histogram of coexisting ZESs [Fig. 9(c)]. Similar studies have been performed on the other two devices and details are presented in Figs. S12– S15

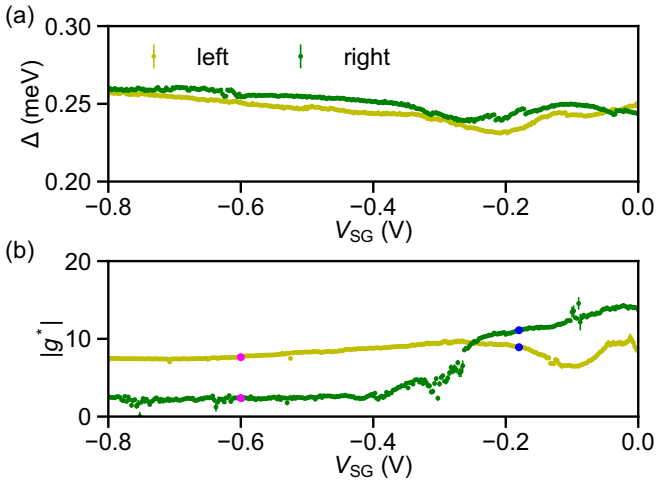

FIG. 8. Gate-dependent induced superconductivity. (a) Superconducting gap as a function of super gate voltage V_{SG} extracted from the left (yellow) and right (green) junction. (b) Effective g factor vs V_{SG} for the left (yellow) and right (green) end of the hybrid nanowire. Magenta and blue points correspond to the data extracted from the traces in Figs. 4(d) and 4(e). g factors are extracted by fitting the linear part of the traces $E_0^{L/R}$ vs $B_{||}$.

in Ref. [35]. The results do not yield evidence for correlated MZMs either.

IV. DISCUSSION

In this work, three-terminal InSb-Al hybrid nanowire devices have been systematically studied using rf reflectometry. This approach introduces a critical experimental technique to quickly map out a large phase space at both ends of superconductor-semiconductor hybrid nanowires, which is crucial for searching for candidate regions of a topological phase. A wide range of chemical potential can be mapped out in high resolution by varying the super gate voltage, and consequently the chance of missing topologically nontrivial regions is minimized. Tunneling spectroscopy depending on super gate voltage and magnetic field enables the extraction of LESs and ZESs, as well as induced superconducting gap and effective g factor. Constructed diagrams of ZESs and LESs indicate the most promising regions for searching for MZMs [27]. Combined with the tunneling-spectroscopy data, clusters of ZPBs, parabolic and oscillatory patterns in ZES and LES diagrams are analyzed for the first time in large scale and high resolution. While such patterns mimic the predicted behavior of MZMs, the systematic exploration of all accessible experimental parameters suggests a nontopological origin. Further analysis by altering barrier gates indicates that the ZESs and LESs observed in this work are likely localized in the vicinity of the tunnel junctions. Additionally, the simultaneous detection of LESs at both ends of the hybrid enables the possibility to look for correlated ZESs, which is a prerequisite to prove the existence of paired MZMs. Yet, the observation of correlated ZBPs can also originate from trivial mechanisms such as Andreev bound states with a long localized length [50]. Even so, no indication of correlated behavior is observed in this work.

The absence of an unbroken topological superconducting phase in these samples can be attributed to several physical origins. Possible reasons include disorder, inhomogeneous interface band bending, local chemical potential fluctuations and a nonperfect detection method. Here, these four possible shortcomings are elaborated. (1) In addition to forming trivial subgap levels which can mimic MZMs, disorder effects could push the Majorana wave functions away from the ends of the hybrid nanowires [20,22]. In this case, even if a topological phase is formed in the bulk, the MZM wave function cannot be probed by tunneling probes at the end of the hybrid nanowire. (2) Local chemical potential fluctuations with an energy above the helical gap can break a single topological phase into segments. In this case, the two ends of a hybrid nanowire are not necessarily correlated. In real devices, such fluctuations can originate from nonuniform gating effects, grain boundaries in aluminium, and disorder from impurities. (3) Recently, the interface band bending between the superconductor and semiconductor was recognized as an important ingredient for tuning the properties of the hybrid [26,40,41]. In particular, band bending can lead to the occupation of multiple subbands, and for the InSb-Al system the experimental implications are still unknown. This makes it difficult to predict the experimental conditions to achieve a topological superconducting phase. (4) The experimental protocol in this work is specifically designed to search for paired MZMs at two ends of an extended topological phase. If for any reason, a topological phase would not be continuous across the entire hybrid, it is possible that MZMs can be probed on one end but not on the other. In this case, the protocol applied in this work would miss a potential topological phase in the parameter space. Such a false negative cannot be ruled out by these measurements. We would note that a more general conclusion, like if topological phase is achievable in InSb-Al hybrid nanowires, cannot be drawn before exploring a large number of such devices to achieve statistical relevance.

For the aforementioned problems, several solutions can be proposed. (1) The InSb nanowires in this work have transport mobilities of $\sim 4 \times 10^4$ cm^2 V^{-1} s^{-1} [32]. The introduction of capping layers on top of the semiconductor could alleviate disorder and improve transport mobilities [51]. (2) In order to improve resilience against local chemical potential fluctuations, alternative superconductors with larger superconducting gaps can be considered. Recent reports have successfully realized growth of Sn ($\Delta \sim 700$ μeV) [52] and Pb ($\Delta \sim 1.25$ meV) [53] on semiconductor nanowires. These hybrids may have a higher chance to achieve an uninterrupted topological phase in spite of the challenges in fabrication. (3) Band bending at the interface between superconductors and semiconductors can be engineered by inserting modulation layers [51]. Simultaneously, proper engineering of these layers can also be used as a tool to influence the magnitude of the induced superconducting gap. (4) Nonlocal measurements, proposed to probe the superconducting gap on three-terminal devices [54], can complement the fast rf reflectometry used in this work [27]. Corresponding experimental work established its capability of detecting bulk properties beyond the local characteristics [55,56], though the measurement speed was slow. Combining our present protocol with nonlocal

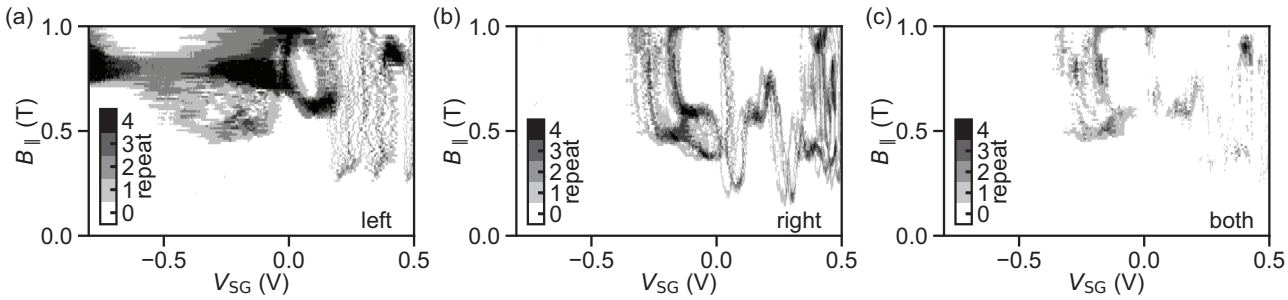

FIG. 9. Overlapping ZES diagrams taken at different barrier gate settings for the left junction (a), right junction (b), and coexistence in both junctions (c). The panels are obtained by overlapping ZES diagrams from Fig. S9 ($g_L \sim 0.027\ G_0$, $g_R \sim 0.025\ G_0$), Fig. S10 ($g_L \sim 0.029\ G_0$, $g_R \sim 0.004\ G_0$), Fig. 4 ($g_L \sim 0.03\ G_0$, $g_R \sim 0.064\ G_0$), and Fig. S11 ($g_L \sim 0.047\ G_0$, $g_R \sim 0.129\ G_0$).

measurement would strike a balance between measurement speed and detection reliability.

The experimental protocol developed in this work, together with possible improvements discussed above, will pave the way for unambiguously detecting MZMs in superconductor-semiconductor hybrid systems in the future.

ACKNOWLEDGMENTS

We thank Michael Wimmer, Daniel Loss, Jelena Klinovaja, and Anton Akhmerov for valuable comments on our manuscript. We also thank John M. Hornibrook and David J. Reilly for providing the frequency multiplexing chips. We are grateful to Raymond Schouten, Olaf Benningshof and J. Mensingh for valuable technical support. This work has been financially supported by the Dutch Organization for Scientific Research (NWO) and Microsoft Corporation Station Q.

Author contribution

J.-Y.W., S.H., and L.P.K. conceived the experiment. J.-Y.W., G.M., N.v.L., M.L., F.B., and M.Q.P. fabricated the devices. J.-Y.W., V.L. and F.K.M. performed the measurements. S.G., G.B., and E.P.A.M.B. carried out the material growth. J.-Y.W. analyzed the data. J.-Y.W., N.v.L., G.P.M, V.L., and L.P.K wrote manuscript with comments from all authors. J.-Y.W., S.H., and L.P.K. supervised the project.

[1] L. Fu and C. L. Kane, Superconducting Proximity Effect and Majorana Fermions at the Surface of a Topological Insulator, Phys. Rev. Lett. **100**, 096407 (2008).

[2] R. M. Lutchyn, J. D. Sau, and S. Das Sarma, Majorana Fermions and a Topological Phase Transition in Semiconductor-Superconductor Heterostructures, Phys. Rev. Lett. **105**, 077001 (2010).

[3] Y. Oreg, G. Refael, and F. von Oppen, Helical Liquids and Majorana Bound States in Quantum Wires, Phys. Rev. Lett. **105**, 177002 (2010).

[4] V. Mourik, K. Zuo, S. M. Frolov, S. R. Plissard, E. P. A. M. Bakkers, and L. P. Kouwenhoven, Signatures of Majorana Fermions in Hybrid Superconductor-Semiconductor Nanowire Devices, Science **336**, 1003 (2012).

[5] M. T. Deng, C. L. Yu, G. Y. Huang, M. Larsson, P. Caroff, and H. Q. Xu, Anomalous Zero-Bias Conductance Peak in a Nb-InSb Nanowire-Nb Hybrid Device, Nano Lett. **12**, 6414 (2012).

[6] A. Das, Y. Ronen, Y. Most, Y. Oreg, M. Heiblum, and H. Shtrikman, Zero-bias peaks and splitting in an Al-InAs nanowire topological superconductor as a signature of Majorana fermions, Nat. Phys. **8**, 887 (2012).

[7] H. O. H. Churchill, V. Fatemi, K. Grove-Rasmussen, M. T. Deng, P. Caroff, H. Q. Xu, and C. M. Marcus, Superconductor-nanowire devices from tunneling to the multichannel regime: Zero-bias oscillations and magnetoconductance crossover, Phys. Rev. B **87**, 241401(R) (2013).

[8] M. T. Deng, S. Vaitiekėnas, E. B. Hansen, J. Danon, M. Leijnse, K. Flensberg, J. Nygård, P. Krogstrup, and C. M. Marcus, Majorana bound state in a coupled quantum-dot hybrid-nanowire system, Science **354**, 1557 (2016).

[9] J. Chen, P. Yu, J. Stenger, M. Hocevar, D. Car, S. R. Plissard, E. P. A. M. Bakkers, T. D. Stanescu, and S. M. Frolov, Experimental phase diagram of zero-bias conductance peaks in superconductor/semiconductor nanowire devices, Sci. Adv. **3**, e1701476 (2017).

[10] H. Zhang, M. W. A. de Moor, J. D. S. Bommer, D. Xu, G. Wang, N. van Loo, C.-X. Liu, S. Gazibegovic, J. A. Logan, D. Car, R. L. M. Op het Veld, P. J. van Veldhoven, S. Koelling, M. A. Verheijen, M. Pendharkar, D. J. Pennachio, B. Shojaei, J. Sue Lee, C. J. Palmstrøm, E. P. A. M. Bakkers, S. Das Sarma, and L. P. Kouwenhoven, Large zero-bias peaks in InSb-Al hybrid semiconductor-superconductor nanowire devices, arXiv:2101.11456 (2021)

[11] S. Vaitiekėnas, G. W. Winkler, B. van Heck, T. Karzig, M.-T. Deng, K. Flensberg, L. I. Glazman, C. Nayak, P. Krogstrup, R. M. Lutchyn, and C. M. Marcus, Flux-induced topological superconductivity in full-shell nanowires, Science **367**, 1442 (2020).

[12] F. Nichele, A. C. C. Drachmann, A. M. Whiticar, E. C. T. O'Farrell, H. J. Suominen, A. Fornieri, T. Wang, G. C. Gardner, C. Thomas, A. T. Hatke, P. Krogstrup, M. J. Manfra, K. Flensberg, and C. M. Marcus, Scaling of Majorana Zero-Bias Conductance Peaks, Phys. Rev. Lett. **119**, 136803 (2017).

[13] A. Fornieri, A. M. Whiticar, F. Setiawan, E. Portolés, A. C. C. Drachmann, A. Keselman, S. Gronin, C. Thomas, T. Wang, R. Kallaher, G. C. Gardner, E. Berg, M. J. Manfra, A. Stern, C. M. Marcus, and F. Nichele, Evidence of topological superconductivity in planar Josephson junctions, Nature (London) **569**, 89 (2019).

[14] H. Ren, F. Pientka, S. Hart, A. T. Pierce, M. Kosowsky, L. Lunczer, R. Schlereth, B. Scharf, E. M. Hankiewicz, L. W. Molenkamp, B. I. Halperin, and A. Yacoby, Topological superconductivity in a phase-controlled Josephson junction, Nature (London) **569**, 93 (2019).

[15] A. Vuik, B. Nijholt, A. R. Akhmerov, and M. Wimmer, Reproducing topological properties with quasi-Majorana states, SciPost Phys. **7**, 061 (2019).

[16] J. Liu, A. C. Potter, K. T. Law, and P. A. Lee, Zero-Bias Peaks in the Tunneling Conductance of Spin-Orbit-Coupled Superconducting Wires with and without Majorana End-States, Phys. Rev. Lett. **109**, 267002 (2012).

[17] H. Pan and S. Das Sarma, Disorder effects on Majorana zero modes: Kitaev chain versus semiconductor nanowire, Phys. Rev. B **103**, 224505 (2021).

[18] H. Pan, C.-X. Liu, M. Wimmer, and S. Das Sarma, Quantized and unquantized zero-bias tunneling conductance peaks in Majorana nanowires: Conductance below and above $2e^2/h$, Phys. Rev. B **103**, 214502 (2021).

[19] H. Pan and S. Das Sarma, Crossover between trivial zero modes in Majorana nanowires, Phys. Rev. B **104**, 054510 (2021).

[20] S. Das Sarma and H. Pan, Disorder-induced zero-bias peaks in Majorana nanowires, Phys. Rev. B **103**, 195158 (2021).

[21] M. Valentini, F. Peñaranda, A. Hofmann, M. Brauns, R. Hauschild, P. Krogstrup, P. San-Jose, E. Prada, R. Aguado, and G. Katsaros, Nontopological zero-bias peaks in full-shell nanowires induced by flux-tunable Andreev states, Science **373**, 82 (2021).

[22] J. Liu, F.-C. Zhang, and K. T. Law, Majorana fermion induced nonlocal current correlations in spin-orbit coupled superconducting wires, Phys. Rev. B **88**, 064509 (2013).

[23] H.-F. Lü, H.-Z. Lu, and S.-Q. Shen, Current noise cross correlation mediated by Majorana bound states, Phys. Rev. B **90**, 195404 (2014).

[24] Y.-H. Lai, J. D. Sau, and S. Das Sarma, Presence versus absence of end-to-end nonlocal conductance correlations in Majorana nanowires: Majorana bound states versus Andreev bound states, Phys. Rev. B **100**, 045302 (2019).

[25] G. L. R. Anselmetti, E. A. Martinez, G. C. M enard, D. Puglia, F. K. Malinowski, J. S. Lee, S. Choi, M. Pendharkar, C. J. Palmstrøm, C. M. Marcus, L. Casparis, and A. P. Higginbotham, End-to-end correlated subgap states in hybrid nanowires, Phys. Rev. B **100**, 205412 (2019).

[26] A. E. Antipov, A. Bargerbos, G. W. Winkler, B. Bauer, E. Rossi, and R. M. Lutchyn, Effects of Gate-Induced Electric Fields on Semiconductor Majorana Nanowires, Phys. Rev. X **8**, 031041 (2018).

[27] D. I. Pikulin, B. van Heck, T. Karzig, E. A. Martinez, B. Nijholt, T. Laeven, G. W. Winkler, J. D. Watson, S. Heedt, M. Temurhan, V. Svidenko, R. M. Lutchyn, M. Thomas, G. de Lange, L. Casparis, and C. Nayak, Protocol to identify a topological superconducting phase in a three-terminal device, arXiv:2103.12217.

[28] A. Wallraff, D. I. Schuster, A. Blais, L. Frunzio, R.- S. Huang, J. Majer, S. Kumar, S. M. Girvin, and R. J. Schoelkopf, Strong coupling of a single photon to a superconducting qubit using circuit quantum electrodynamics, Nature (London) **431**, 162 (2004).

[29] J. M. Hornibrook, J. I. Colless, A. C. Mahoney, X. G. Croot, S. Blanvillain, H. Lu, A. C. Gossard, and D. J. Reilly, Frequency multiplexing for readout of spin qubits, Appl. Phys. Lett. **104**, 103108 (2014).

[30] D. Razmadze, D. Sabonis, F. K. Malinowski, G. C. Ménard, S. Pauka, H. Nguyen, D. M. T. van Zanten, E. C. T. O'Farrell, J. Suter, P. Krogstrup, F. Kuemmeth, and C. M. Marcus, Radio-Frequency Methods for Majorana-Based Quantum Devices: Fast Charge Sensing and Phase-Diagram Mapping, Phys. Rev. Applied **11**, 064011 (2019).

[31] J. van Veen, D. de Jong, L. Han, C. Prosko, P. Krogstrup, J. D. Watson, L. P. Kouwenhoven, and W. Pfaff, Revealing charge-tunneling processes between a quantum dot and a superconducting island through gate sensing, Phys. Rev. B **100**, 174508 (2019).

[32] G. Badawy, S. Gazibegovic, F. Borsoi, S. Heedt, C.-A. Wang, S. Koelling, M. A. Verheijen, L. P. Kouwenhoven, and E. P. A. M. Bakkers, High mobility stemless InSb nanowires, Nano Lett. **19**, 3575 (2019).

[33] S. Heedt, M. Quintero-Pérez, F. Borsoi, A. Fursina, N. van Loo, G. P. Mazur, M. P. Nowak, M. Ammerlaan, K. Li, S. Korneychuk, J. Shen, M. An Y. van de Poll, G. Badawy, S. Gazibegovic, N. de Jong, P. Aseev, K. van Hoogdalem, E. P. A. M. Bakkers, and L. P. Kouwenhoven, Shadow-wall lithography of ballistic superconductor-semiconductor quantum devices, Nat. Commun. **12**, 4914 (2021).

[34] F. Borsoi, G. P. Mazur, N. van Loo, M. P. Nowak, L. Bourdet, K. Li, S. Korneychuk, A. Fursina, J.-Y. Wang, V. Levajac, E. Memisevic, G. Badawy, S. Gazibegovic, K. van Hoogdalem, E. P. A. M. Bakkers, L. P. Kouwenhoven, S. Heedt, and M. Quintero-Pérez, Single-shot fabrication of semiconducting-superconducting nanowire devices, Adv. Funct. Mater. **31**, 2102388 (2021).

[35] See Supplemental Material at http://link.aps.org/supplemental/10.1103/PhysRevB.106.075306 for a parametric exploration of zero-energy modes in three-terminal InSb-Al nanowire devices. The Supplemental Material includes a reference to M. S. Khalil, M. J. A. Stoutimore, F. C. Wellstood, and K. D. Osborn, An analysis method for asymmetric resonator transmission applied to superconducting devices, J. Appl. Phys. **111**, 054510 (2012).

[36] R. J. Schoelkopf, P. Wahlgren, A. A. Kozhevnikov, P. Delsing, and D. E. Prober, The radio-frequency single-electron transistor (RF-SET): A fast and ultrasensitive electrometer, Science **280**, 1238 (1998).

[37] D. J. Reilly, C. M. Marcus, M. P. Hanson, and A. C. Gossard, Fast single-charge sensing with a RF quantum point contact, Appl. Phys. Lett. **91**, 162101 (2007).

[38] J. Stehlik, Y.-Y. Liu, C. M. Quintana, C. Eichler, T. R. Hartke, and J. R. Petta, Fast Charge Sensing of a Cavity-Coupled Double Quantum Dot Using a Josephson Parametric Amplifier, Phys. Rev. Applied **4**, 014018 (2015).

[39] J. Shen, G. W. Winkler, F. Borsoi, S. Heedt, V. Levajac, J.-Y. Wang, D. van Driel, D. Bouman, S. Gazibegovic, R. L. M. Op Het Veld, D. Car, J. A. Logan, M. Pendharkar, C. J. Palmstrøm,

E. P. A. M. Bakkers, L. P. Kouwenhoven, and B. van Heck, Full parity phase diagram of a proximitized nanowire island, Phys. Rev. B **104**, 045422 (2021).

[40] C. Reeg, D. Loss, and J. Klinovaja, Metallization of a Rashba wire by a superconducting layer in the strong-proximity regime, Phys. Rev. B **97**, 165425 (2018).

[41] A. E. G. Mikkelsen, P. Kotetes, P. Krogstrup, and K. Flensberg, Hybridization at Superconductor-Semiconductor Interfaces, Phys. Rev. X **8**, 031040 (2018).

[42] C. Reeg, O. Dmytruk, D. Chevallier, D. Loss, and J. Klinovaja, Zero-energy Andreev bound states from quantum dots in proximitized Rashba nanowires, Phys. Rev. B **98**, 245407 (2018).

[43] S. Das Sarma, J. D. Sau, and T. D. Stanescu, Splitting of the zero-bias conductance peak as smoking gun evidence for the existence of the Majorana mode in a superconductor-semiconductor nanowire, Phys. Rev. B **86**, 220506(R) (2012).

[44] E. J. H. Lee, X. Jiang, M. Houzet, R. Aguado, C. M. Lieber, and S. De Franceschi, Spin-resolved Andreev levels and parity crossings in hybrid superconductor-semiconductor nanostructures, Nat. Nanotechnol. **9**, 79 (2014).

[45] M. W. A. de Moor, J. D. S. Bommer, D. Xu, G. W. Winkler, A. E. Antipov, A. Bargerbos, G. Wang, N. van Loo, R. L. M. Op het Veld, S. Gazibegovic, D. Car, J. A. Logan, M. Pendharkar, J. Sue Lee, E. P. A. M. Bakkers, C. J. Palmstrøm, R. M. Lutchyn, L. P. Kouwenhoven, and H. Zhang, Electric field tunable superconductor-semiconductor coupling in Majorana nanowires, New J. Phys. **20**, 103049 (2018).

[46] R. C. Dynes, V. Narayanamurti, and J. P. Garno, Direct Measurement of Quasiparticle-Lifetime Broadening in a Strong-Coupled Superconductor, Phys. Rev. Lett. **41**, 1509 (1978).

[47] S. Vaitiekėnas, M.-T. Deng, J. Nygård, P. Krogstrup, and C. M. Marcus, Effective g Factor of Subgap States in Hybrid Nanowires, Phys. Rev. Lett. **121**, 037703 (2018).

[48] O. Dmytruk, D. Chevallier, D. Loss, and J. Klinovaja, Renormalization of the quantum dot g factor in superconducting Rashba nanowires, Phys. Rev. B **98**, 165403 (2018).

[49] C.-X. Liu, J. D. Sau, T. D. Stanescu, and S. Das Sarma, Andreev bound states versus Majorana bound states in quantum dot-nanowire-superconductor hybrid structures: Trivial versus topological zero-bias conductance peaks, Phys. Rev. B **96**, 075161 (2017).

[50] R. Hess, H. F. Legg, D. Loss, and J. Klinovaja, Local and nonlocal quantum transport due to Andreev bound states in finite Rashba nanowires with superconducting and normal sections, Phys. Rev. B **104**, 075405 (2021).

[51] J. Shabani, M. Kjaergaard, H. J. Suominen, Y. Kim, F. Nichele, K. Pakrouski, T. Stankevic, R. M. Lutchyn, P. Krogstrup, R. Feidenhans'l, S. Kraemer, C. Nayak, M. Troyer, C. M. Marcus, and C. J. Palmstrøm, Two-dimensional epitaxial superconductor-semiconductor heterostructures: A platform for topological superconducting networks, Phys. Rev. B **93**, 155402 (2016).

[52] M. Pendharkar, B. Zhang, H. Wu, A. Zarassi, P. Zhang, C. P. Dempsey, J. S. Lee, S. D. Harrington, G. Badawy, S. Gazibegovic, R. L. M. Op het Veld, M. Rossi, J. Jung, A.-H. Chen, M. A. Verheijen, M. Hocevar, E. P. A. M. Bakkers, C. J. Palmstrøm, and S. M. Frolov, Parity-preserving and magnetic field-resilient superconductivity in InSb nanowires with Sn shells, Science **372**, 508 (2021).

[53] T. Kanne, M. Marnauza, D. Olsteins, D. J. Carrad, J. E. Sestoft, J. de Bruijckere, L. Zeng, E. Johnson, E. Olsson, K. Grove-Rasmussen, and J. Nygård, Epitaxial Pb on InAs nanowires for quantum devices, Nat. Nanotechnol. **16**, 776 (2021).

[54] T. Ö. Rosdahl, A. Vuik, M. Kjaergaard, and A. R. Akhmerov, Andreev rectifier: A nonlocal conductance signature of topological phase transitions, Phys. Rev. B **97**, 045421 (2018).

[55] G. C. Ménard, G. L. R. Anselmetti, E. A. Martinez, D. Puglia, F. K. Malinowski, J. S. Lee, S. Choi, M. Pendharkar, C. J. Palmstrøm, K. Flensberg, C. M. Marcus, L. Casparis, and A. P. Higginbotham, Conductance-Matrix Symmetries of a Three-Terminal Hybrid Device, Phys. Rev. Lett. **124**, 036802 (2020).

[56] D. Puglia, E. A. Martinez, G. C. Ménard, A. Pöschl, S. Gronin, G. C. Gardner, R. Kallaher, M. J. Manfra, C. M. Marcus, A. P. Higginbotham, and L. Casparis, Closing of the induced gap in a hybrid superconductor-semiconductor nanowire, Phys. Rev. B **103**, 235201 (2021).